

# Journal of Applied Remote Sensing

RemoteSensing.SPIEDigitalLibrary.org

## Characterization of natural and manmade targets from L-band ground-based polarimetric synthetic aperture radar data

Sevket Demirci  
Betul Yilmaz  
Hakan Isiker  
Serhat Gokkan  
Caner Ozdemir

**SPIE.**

Sevket Demirci, Betul Yilmaz, Hakan Isiker, Serhat Gokkan, Caner Ozdemir, "Characterization of natural and manmade targets from L-band ground-based polarimetric synthetic aperture radar data," *J. Appl. Remote Sens.* **13**(4), 044512 (2019), doi: 10.1117/1.JRS.13.044512.

# Characterization of natural and manmade targets from L-band ground-based polarimetric synthetic aperture radar data

Sevket Demirci,<sup>a,\*</sup> Betul Yilmaz,<sup>a</sup> Hakan Isiker,<sup>b</sup> Serhat Gokkan,<sup>b</sup> and Caner Ozdemir<sup>a</sup>

<sup>a</sup>Mersin University, Department of Electrical-Electronics Engineering, Yenisehir, Mersin, Turkey

<sup>b</sup>Mersin University, Vocational School of Technical Sciences, Yenisehir, Mersin, Turkey

**Abstract.** Characterization of polarimetric backscattering phenomenon is investigated through the ground-based synthetic aperture radar (GB-SAR) data that are collected from a test site consisting of manmade targets distributed over a vegetated terrain at L-band frequencies. The characterization of either synthetic or natural targets has been made by applying two main polarization interpretation schemes, namely amplitude-based interpretation and target-based interpretation in extracting the features of those targets. Polarimetric backscattering signatures of objects are analyzed by assessing the Pauli, total power, entropy/mean-alpha ( $H/\bar{\alpha}$ ) images of the terrain for the goal of identification and classification of scattering mechanisms. After applying the classification methodology presented, obtained polarimetric images have demonstrated that target features can be effectively discriminated from each other providing a successful characterization of natural and manmade objects based on GB-SAR measurements. Specifically,  $H/\bar{\alpha}$  classification results are shown to be well capable of clearly identifying the distinct scattering mechanisms of the terrain. Full-polarimetric measurements of this particular scene confirmed the ability to retrieve the physical target features to a certain extent using the high-resolution GB-SAR imagery and the relevant polarimetric analyses. © 2019 Society of Photo-Optical Instrumentation Engineers (SPIE) [DOI: [10.1117/1.JRS.13.044512](https://doi.org/10.1117/1.JRS.13.044512)]

**Keywords:** synthetic aperture radar (SAR); radar polarimetry; ground-based SAR; polarimetric SAR.

Paper 190189 received Mar. 14, 2019; accepted for publication Oct. 10, 2019; published online Oct. 29, 2019.

## 1 Introduction

For the past half century, synthetic aperture radar (SAR) imaging has been an effective microwave remote sensing tool with the ultimate aim of retrieving quantitative physical information about the Earth's surface and targets on it. Progress toward this aim, however, has been impeded in many instances due to the complexity of interaction mechanisms between microwaves and natural media that is highly dependent on numerous factors such as target and radar parameters. For this reason, it is not always easy to fully evaluate the overall success and validity of the obtained SAR image results. To overcome this limitation and utilize the apparent benefits of diversity, modern SAR acquisition systems are now providing multifrequency, multispatial, multipolarization, and multitemporal data. Accordingly, several types of SAR techniques, including polarimetric SAR (PolSAR), interferometric SAR (InSAR), differential SAR interferometry (DInSAR), polarimetric SAR interferometry (POInSAR), and tomographic SAR (TomoSAR) have been established, each of which has different applications and technical equipment.<sup>1,2</sup> Thanks to recent improvements on the radar hardware technologies, they all can be operated from the space, air, or on the ground.

Compared to space-borne or air-borne systems, ground-based radar systems offer one practical means of monitoring relatively small spatial-scale areas. Excluding nonimaging

---

\*Address all correspondence to Sevket Demirci, E-mail: [sdemirci@mersin.edu.tr](mailto:sdemirci@mersin.edu.tr)

scatterometers,<sup>3-7</sup> ground-based synthetic aperture radar (GB-SAR) typically uses precisely controlled vehicle<sup>8-11</sup> or rail-based<sup>12-51</sup> scanning set-ups to synthesize the along-track aperture. This eliminates data processing complications such as inaccurate raw data due to the motion effects, as encountered in satellite, aircraft, or UAV-based SAR missions. In addition, it also provides low-cost, rapid operation and can easily be adapted to different observation geometries. For these reasons, various studies employing different frequencies and radar waveforms have deployed GB-SAR in selected topics of research to determine and demonstrate its usage and applicability. For the recent years, GB-SAR approach has been found to be a useful and desirable tool for research and validation, as well as for monitoring the dynamics of terrain over short sampling durations. Below are the important usages of its employment in various fields:

- surface topography mapping with InSAR;<sup>12-15</sup>
- monitoring of ground displacement and deformation with DInSAR<sup>16-25</sup> and polarimetric DInSAR;<sup>26-32</sup>
- snow and ice profiling with TomoSAR;<sup>33-35</sup>
- mapping of soil surface roughness and moisture with single-polarization SAR;<sup>36,37</sup>
- characterization of crops with PolSAR<sup>38,39</sup> and PolInSAR;<sup>40</sup>
- ground-truth validation of tree scattering with single-polarization SAR<sup>41</sup> and polarimetric TomoSAR;<sup>42-44</sup>
- investigation of a mixture of manmade, urban, and natural structures with single-polarization SAR,<sup>8-11,45,46</sup> PolSAR,<sup>47,48</sup> TomoSAR,<sup>49,50</sup> and polarimetric TomoSAR.<sup>51</sup>

As far as PolSAR is concerned, it is well known that radar polarimetry is sensitive to structure (e.g., orientation, shape, and size) and dielectric properties of the scatterer. This allows extraction and separation of different scattering mechanisms via decomposition techniques. It becomes, therefore, possible to distinguish different targets in the scene and estimate their physical parameters using this information. To date, many documented successful images of PolSAR have been reported for specific space and air-based applications.<sup>1,2</sup> On the other hand, the method does not always lead to clearly interpreted results such that additional ground-based surveys are needed for better utilizing its potential in target parameter retrieval in most scenarios. This is mainly related to the lack of ground-truth data in majority of air- or space-borne SAR missions. Consequently, the GB-SAR studies itemized above have been going more to the cases of polarimetric information merging it with time and incidence (i.e., spatial) diversity as well. The reader is encouraged to refer to Refs. 26-28, 31, 32, 42, 48, and 51 for some interesting applications of ground-based PolSAR applications over different land cases. At present, polarimetry is playing a leading role in the success of most SAR missions, and additional ground-based surveys are needed for better exploiting its potential in target parameter extraction.

In this context, the main objective of this paper is to investigate the polarimetric characteristics of different terrain targets such as trees, grass, and various manmade structures by assessing the fully polarimetric L-band GB-SAR measured images and to reveal and confirm the polarimetric backscattering signatures of those targets. Such an investigation allows also an evaluation of the validity of the relevant polarimetric analysis techniques. For this purpose, an experiment was conducted for the test site consisted of a soil surface with slight and no vegetation cover zones, small plants, trees, and artificial objects such as a parking lot, a car, and a signboard. Trihedral corner reflectors (TCRs) were also put to the scene because of their usage as pilot targets in SAR applications.<sup>52</sup>

The high-resolution GB-SAR image signatures of different elements are analyzed to characterize their polarimetric scatterings thereby interpreting their physical features. The characterization of both natural and synthetic and natural targets is made by applying two kinds of polarimetric interpretation schemes, namely interpretation based on amplitude data and interpretation based on target decomposition techniques. After accomplishing an elementary analysis of the amplitude and the Pauli decomposition images, a detailed investigation is made using the eigenvalue/eigenvector decomposition of the coherency matrix. The image products (e.g., entropy and alpha) derived from this decomposition and the unsupervised  $H/\bar{\alpha}$  classification image are examined in accordance with the apparent scattering mechanisms expected within the scene. In particular, the  $H/\bar{\alpha}$  classification image described the targets' scattering properties more precisely and distinguished between the targets that are manmade, dense vegetation,

slightly vegetated (surface), and other regions of interest. The findings of these interpretations and the detailed discussions are presented.

## 2 Methodology and Characteristics of GB-SAR

### 2.1 Data Collection Geometry

Figure 1(a) illustrates the geometry for a two-dimensional (2-D) monostatic GB-SAR imaging system. The radar antenna located at a height  $h$  and inclined with an incidence angle  $\beta'$  from the vertical direction, illuminates the target area described by reflectivity  $F(x, y)$  with a desired range of local incidence angles  $\beta$  (or local grazing angles  $\alpha$ ). Backscattered electric field data are acquired with  $\Delta x$  azimuth steps by moving the antenna along a synthetic aperture length of  $L = N \cdot \Delta x$ , where  $N$  is the total number of spatial samples. The axes perpendicular and parallel to the scanning direction are called ground range  $y$  and cross range  $x$ , respectively. The slant range  $r$  refers to the true target distance that is related to ground range as  $y = r \cdot \sin(\beta)$ .

### 2.2 Range Characteristics

As sketched in Fig. 1(b), the range extent of the footprint is settled by the nearest  $r_{\min}$  and the farthest  $r_{\max}$  range limits and depends on  $h$ ,  $\beta'$ , and the antenna's  $-3$  dB elevation beamwidth  $\Phi_{3\text{dB}}$ . The maximum unambiguous range  $R_{\max}$  can be chosen within this extent. Then the frequency step size  $\Delta f$  can be set to  $\Delta f \leq c/2R_{\max}$  for a stepped-frequency continuous wave operation. Here  $c$  is the speed of light in the air. The range resolution  $\delta_r$  depends on the frequency bandwidth  $B$  through the well-known formula of  $\delta_r = c/2B$ . Furthermore, the ground-range resolution  $\delta_y$  can be identified by  $\delta_y = \delta_r / \sin \beta$ , which implies that nearer points are better resolved than the farther ones as expected.

### 2.3 Cross-Range Characteristics

Figure 1(c) shows the top view geometry for the illustration of cross-range characteristics. The extent of the footprint is determined by the radar antenna's azimuth beam-width  $\theta_{3\text{dB}}$ , and it spreads out along cross-range axis as range of the target increases. The influences of different parameters for a successful GB-SAR imaging operation is explained as follows: first, the desired image size with a range depth  $D$  and a cross-range width  $W$  are chosen and the center of the synthetic aperture length  $L$  is set, usually but not necessarily with respect to the image center. Next, noting that the highest spatial frequency along  $x$  direction is limited by  $W$ , the sampling criterion for  $\Delta x$  is calculated from the below inequality:

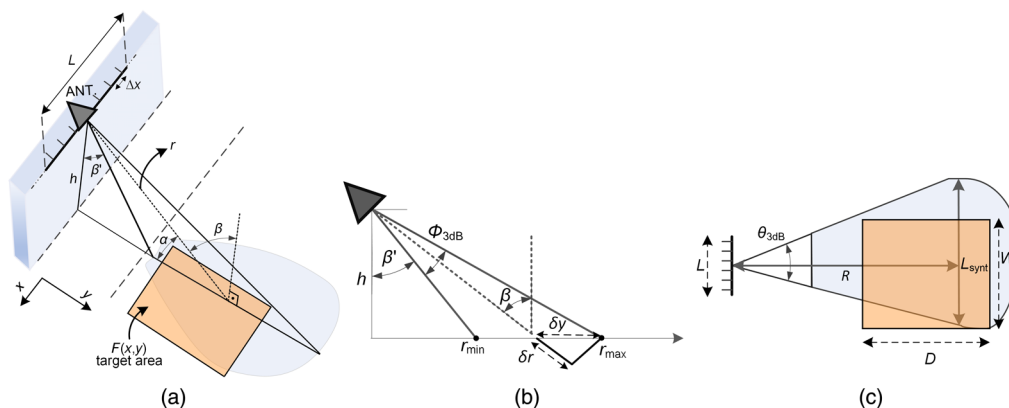


**Fig. 1** Data collection geometry for a 2-D GB-SAR imaging system: (a) perspective view, (b) side view, and (c) top view.

$$\Delta x \leq \frac{\lambda_{\min} R_{\min}}{W}, \quad (1)$$

where  $\lambda_{\min}$  is the minimum transmitted wavelength and  $R_{\min}$  is the distance of the nearest point to the aperture center. After determining  $\Delta x$ , the value of  $L$  can be decided by considering the highest possible cross-range resolution  $\delta_x$ , given  $W$  and the practical constraints in scanning. This can be clarified from the angular domain view of data collection in the following manner: throughout the sampling points on  $L$ , the scene is observed with a set of look angles from radar to the image center. The span of these angles labeled as  $\Delta\theta$  defines the cross-range resolution and depends on the value of  $L$ . The longer the  $L$  means the larger the  $\Delta\theta$  and thus the better  $\delta_x$ . For a strip-map SAR operation, the optimal synthetic aperture length  $L_{\text{synt}}$  is achieved when  $\Delta\theta$  is set to  $\theta_{-3 \text{ dB}}$  for which the highest resolution is attained, i.e.,  $\delta_x = D_{\text{ant}}/2$ , where  $D_{\text{ant}}$  is the maximum size of the antenna aperture. For a given range  $R$ ,  $L_{\text{synt}}$  can be calculated from

$$L_{\text{synt}} \cong R\theta_{3 \text{ dB}} = \frac{R\lambda}{D_{\text{ant}}}. \quad (2)$$

In most GB-SAR measurements, it is difficult to cover this maximum aperture, that is  $L < L_{\text{synt}}$ , leading to suboptimal resolutions varying with range  $R$  as

$$\delta_x = \frac{R\lambda}{2L}. \quad (3)$$

Also the far-field radiation condition, i.e.,  $R_{\min} \geq 2W^2/\lambda_{\min}$  is not met in practice, implying the requirement of a near-field reconstruction algorithm.

## 2.4 Effect of Incidence Angle on Backscatter Power

Ranges in GB-SAR systems are usually very short due to its nature of low-altitude operation. Thus targets are observed with relatively high values of incidence angle  $\beta$ . Noting that scattering mechanisms and intensities depend strongly on incidence angle, this can provide either advantageous or disadvantageous situation. For example, considering the scattering from a natural surface with a roughness measure of height  $h$ , the surface is regarded as smooth on a wavelength scale if the Rayleigh criterion

$$h < \frac{\lambda}{8 \cos \beta} \quad (4)$$

is met. Then quasispecular reflection with low backscattering energy results in the case of a monostatic radar. Evidently, the likelihood of having a specular reflection rises with increasing incidence angles, which is more likely to occur in GB-SAR geometries for a given surface roughness. Therefore, high-contrast differences between the image signatures of smooth surfaces and low-vegetation areas can be expected at larger incidence angles, which aids in their proper discrimination. Moreover, volume scattering from trees and other heterogeneous regions also tends to provide good isolation from the underlying surface at larger incidence angles. This can be also useful in detecting clear-cuts, roads, bare soil regions within a forest environment. As for the manmade land surfaces such as paved roads, electromagnetic backscattering is usually less sensitive to incidence angle, giving mostly specular returns for commonly used microwave frequency bands.

## 2.5 Effect of Polarization on Backscatter Power

In addition to angular dependency, backscattered power is also a function of the polarizations of the transmitted and received electromagnetic waves. Most polarimetric radars operate in linear horizontal (H)–vertical (V) basis, measuring up to four channels, i.e., HH, VV, HV, and VH with the first and second letters represent transmit and receive polarizations, respectively.

It is well known that canonical targets generate a completely deterministic (i.e., nondepolarizing) scattering signatures, and they can be specially constructed and oriented to produce high-energy levels within the desired polarization channels.<sup>52</sup> For example, TCRs produce high co-polar (HH and VV) and ideally zero cross-polar (HV and VH) returns, as stated from the scattering matrix of a TCR

$$[S_{\text{TCR}}] = \begin{bmatrix} S_{\text{HH}} & S_{\text{HV}} \\ S_{\text{VH}} & S_{\text{VV}} \end{bmatrix} = A \begin{bmatrix} 1 & 0 \\ 0 & 1 \end{bmatrix}, \quad (5)$$

where  $A = A_0 e^{j\varphi_0}$  is a constant. The elements of the scattering matrix  $[S]$  are known as the complex scattering amplitudes and are not related to each other except through the scattering process at the target. Each pixel in an SAR image retains this single complex number, which is a proportional compound of the superposition of different scattering contributions within one resolution cell. For deterministic targets, both the amplitude and phase data can be directly used to acquire the knowledge about the features of targets. For distributed targets, however, there exist many point scatterers inside one resolution cell, which gives rise to uniformly distributed random phase that is not relevant for direct use. In such cases, spatial averaging over many resolution cells is required to make use of the phase information. The amplitude data were of main concern for the initial SAR systems, though their information content still need investigations for certain applications.

Real targets, either manmade or natural, depolarize the incident wave to different directions so that the reflected wave has both H and V polarized contributions within the returned signal. This randomness of scattering occurs due to the complex structures that gives rise to multiple reflections or diffuse scattering mechanisms. For surface scattering, quasispecular (coherent) reflection yields high co-polar returns whereas diffuse (random) scattering owing to surface roughness yields high cross-polar returns. For volume scattering, both single (or multiple) reflections and diffuse scattering mechanisms yield high-power levels in all polarization channels.

## 2.6 Polarimetric Image Interpretation

In this study, we aim to make a physical interpretation of a typical land scene by means of polarimetric GB-SAR imaging, thereby evaluating the validity of some relevant PolSAR techniques. Several approaches and methods are possible for the interpretation of polarimetric images.<sup>53,54</sup> As illustrated in Fig. 2, our characterization approach progresses along two different branches of classification techniques explicitly: interpretation based on amplitude images and interpretation based on decomposition images. Both are briefly summarized below for the monostatic data collection scheme.

The most basic information on the scattering objects can be readily obtained by visually interpreting the amplitude images. The amplitudes of each pixels (e.g.,  $|S_{\text{HH}}|$ ) represent the magnitude of the radar backscatter, which depends on the SAR geometry, frequency, polarization, and electrical properties of the scatterer. Considering the changes in the intensity, the type and some properties of the materials at various locations can be identified. For example, relatively high intensity of cross-polarized return is typically associated with volume or multiple scattering from trees and vegetation. For this interpretation, first a normalization procedure should be applied to each polarization images to be able to associate each polarization images with each other. Then a resolution analysis can be utilized to compare obtained resolution values to the expected theoretical ones. Finally, the total power images are retrieved to be able to show how each polarization image's power is linked to polarization sensitive targets. All above analyses are done for the amplitude-based interpretation approach as listed in Fig. 2.

Furthermore, deeper information on the physical properties of objects can be obtained via a quantitative analysis based on complex image data. In particular, the so-called target (or polarimetric scattering) decomposition (right branch in Fig. 2) is capable of separating and classifying the scattering mechanisms present in the scene and thus remains the most active research area in PolSAR information extraction. Target decomposition interpretation can also be categorized into two: coherent decomposition<sup>55-57</sup> and incoherent decomposition.<sup>53-56</sup> The former is better suited

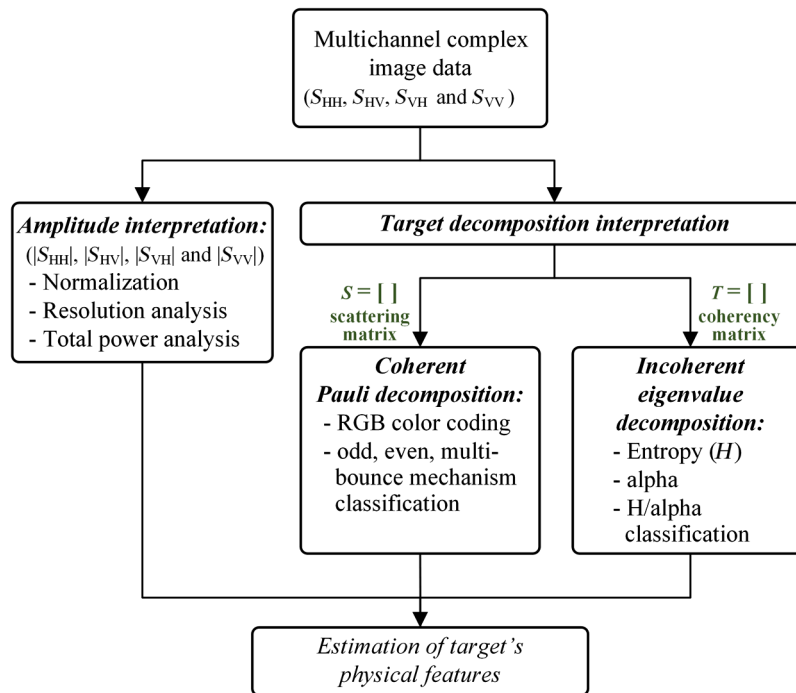


**Fig. 2** Methodological flowchart of the polarimetric analyses used in this study.

to coherent (deterministic) targets, the scattering matrices of which can be directly expressed with a combination of the scattering responses of canonical objects. For example, the Pauli decomposition, mostly deployed in urban applications,  $[S]$  is typically represented with three components that are usually interpreted in terms of an odd-bounce scatterer such as a sphere or a TCR, a dihedral, and a 45-deg inclined dihedral. The latter, on the other hand, is the preferred method to describe the scattering behavior of distributed (natural) targets that induce depolarization of the transmitted wave due to the speckle phenomenon. In this case, the analysis should be performed by means of the second-order descriptors, which are the  $3 \times 3$  average, covariance  $\langle[C]\rangle$ , and coherency  $\langle[T]\rangle$  matrices. In general, the decomposition of these matrices is further rendered into two classes: the eigenvector/eigenvalue-based decomposition<sup>55</sup> and the model-based decompositions.<sup>58</sup> In particular, the former is based on the calculation of the eigenvectors and eigenvalues of the coherency matrix  $\langle[T]\rangle$  from which the parameters of polarimetric entropy, anisotropy, and alpha angle can be calculated. The  $H/\bar{\alpha}$  classification<sup>59</sup> can also be performed using these derived parameters. As shown via the flowchart in Fig. 2, we aimed in this study to exploit both the amplitude-based and target decomposition-based decomposition approaches for the estimation of the targets' physical parameters.

### 3 Experiment Description

#### 3.1 GB-SAR System

Our constructed experimental system consists of a stepped-frequency radar instrument, two linearly polarized Vivaldi horn antennas, a computer, and a radio frequency (RF) amplifier. The whole system was mounted on a wheel platform, which can be discretely moved along a linear trajectory. The radar unit is the Agilent E5071B vector network analyzer (VNA) that has a maximum operation frequency of 8.5 GHz. The antennas are functioning between 300 and 3300 MHz and spaced 30 cm apart in a quasimonostatic arrangement that can be lifted up to a desired height and look angle. The 1-W RF amplifier is inserted between the VNA and the transmitting antenna. All electronic and mechanical operations were controlled by a computer with a MATLAB<sup>60</sup> script.

### 3.2 Test Site

The field experiment was performed in accordance with the GB-SAR geometry given in Fig. 1. A terrain surrounding a building in our campus area was selected as seen in Fig. 3, and the measurements were performed on the building's roof terrace, which is  $\sim 23$  m above the ground level. The target area of interest was comprised of a vegetated land, dirt roads, a parking lot, various manmade items, and add-on TCR targets. The reflectors were placed onto different ground sections and inclined with a zero angle with respect to the ground surface. Four TCRs (T1 to T4) were of triangular type, whereas T5 was of a square type, all of which have equal side lengths  $a$  with values of  $a_{T1} = a_{T2} = 35$  cm,  $a_{T3} = a_{T4} = 70$  cm, and  $a_{T5} = 18$  cm. Among the manufactured objects were a car, a lighting pole, a signboard, two tall vertical metal objects, and various small sized materials positioned mostly within the parking lot. The region covered by vegetation was a scattered compound of grasses, plants, trees, and bare soil sections.

### 3.3 Measurement Parameters

It is important to note that, in monostatic configurations, where transmitter and receiver are co-located,  $S_{HV} = S_{VH}$  for all reciprocal scattering media. Thus we have collected data in three different polarization channels ( $S_{HH}$ ,  $S_{VV}$ , and  $S_{VH}$ ) and for the parameter values given in Table 1. The frequency span was selected as 0.75 – 2.25 GHz with 1601 sampling points yielding a maximum range of  $R_{\max} = 160$  m. The antennas were placed at a height of 24 m and inclined 9 deg from the true azimuth, i.e.,  $\beta' = 81$  deg. Thus knowing that  $\phi_{3\text{ dB}} = 38$  deg at the center frequency of the radar, the range extent was purposely constrained between

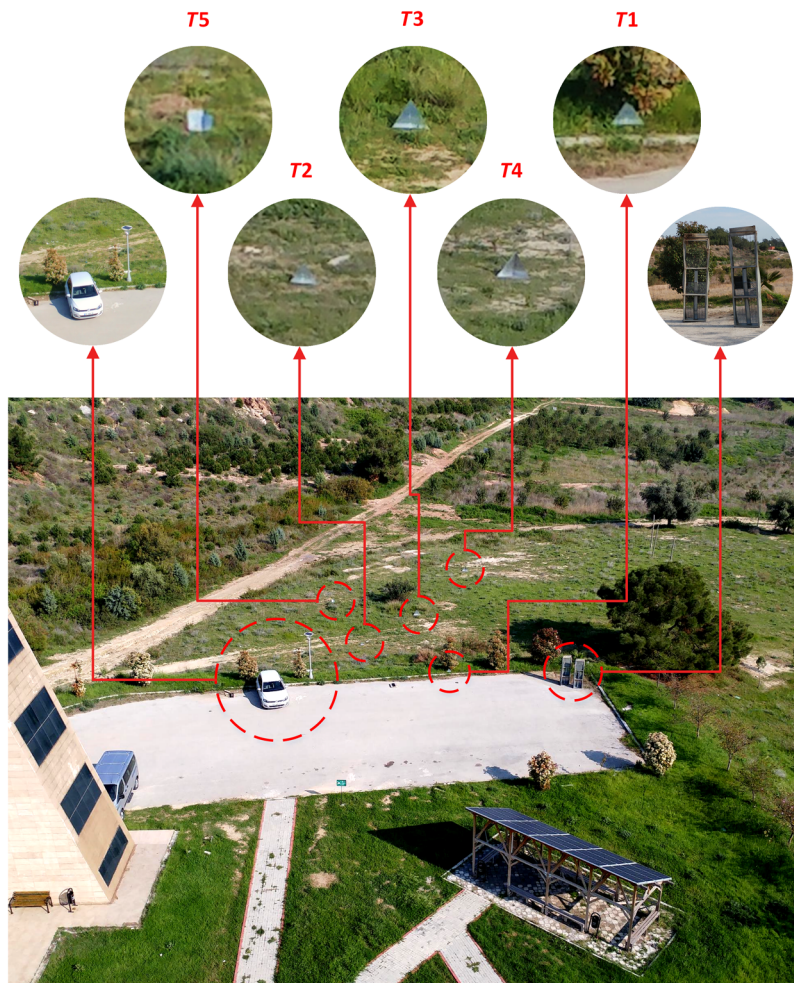


**Fig. 3** Test site with reflector targets as seen from the radar location.

**Table 1** Measurement parameters.

Description	Parameter	Value
Transmission power	$P_0$	30 dBm
Frequency range	$f$	0.75 to 2.25 GHz
Number of frequency samples	$N$	1601
Range extent	$(R_{\min}, R_{\max})$	(22, 152) m
Antenna dimension	$D_{\text{ant}}$	30 cm
Antenna beam widths	$\theta_{3 \text{ dB}}, \phi_{3 \text{ dB}}$	38 deg at 1.5 GHz
Antenna height and incidence angle	$h, \beta'$	24 m, 81 deg
Synthetic aperture step and length	$\Delta x, L$	10 cm, 13.1 m,

22 and 152 m in order to cover the various target ranges of interest. The corresponding local incidence angle  $\beta$  was varying between 43 deg (at  $r_{\min}$ ) and 81 deg (at  $r_{\max}$ ).

The synthetic aperture length  $L$  was first set to the maximum available scanning length of 13.1 m and its midpoint was taken as the cross-range center. The sampling spacing was then decided to be  $\Delta x = 10$  cm, which satisfies the inequality in Eq. (1) for the values of  $f_{\min} = 0.75$  GHz,  $R_{\min} = 22$  m and a typical image width of  $W = 60$  m. It is also worth noting that the cross-range extent of the radar footprint (i.e.,  $L_{\text{synt}}$ ) was changing between 14.6 and 101.3 m corresponding to the ranges 22 to 152 m, respectively [see Eq. (2)]. Therefore, the chosen value of  $L$  is suboptimal, i.e.,  $L < L_{\text{synt}}$  over the imaged area, meaning that cross-range resolution values would be lower than its optimal value of  $D_{\text{ant}}/2$ , which is 15 cm for the current antenna.

## 4 Results and Discussion

The quality of the collected data was first assessed by processing the image signatures of reflector targets. The amplitude and phase imbalances between polarimetric channels were found to be at fairly low levels that imply a reasonable polarization isolation. For this reason and also noting its complexity for GB-SAR systems, the polarimetric calibration was not considered in this study.

In the following, we are going to first discuss the evaluation of intensity images and then the results of various polarimetric analyses based on methodology that is given in Fig. 2.

### 4.1 Intensity Images

The collected data were focused with a near-field back-projection imaging algorithm<sup>61,62</sup> to account for the spherical wave front effects. Figure 4 shows the intensity images for co-polar ( $S_{\text{HH}}$  and  $S_{\text{VV}}$ ) and cross-polar ( $S_{\text{VH}}$ ) channels. The layout of the terrain can be easily noticed in all images. Spotting the values of the two critical parameters,  $13 \leq \lambda \leq 40$  cm and  $42.5 \text{ deg} \leq \beta \leq 80.9 \text{ deg}$ , the following observations can be made: First, considering the responses of reflectors of which locations are pinpointed in Fig. 4(a), they mostly produce large co-polar components, as expected. The levels of  $|S_{\text{HH}}|$  and  $|S_{\text{VV}}|$  channels are very similar, with that of  $|S_{\text{HH}}|$  being somewhat a little bit larger. The three TCRs (T2 to T4) lie on almost open surfaces (see Fig. 3) and produce relatively high backscattering levels, as a result. Nevertheless, the TCR closest to the radar (T1) is not so clearly discriminated. This is related to a nearby small tree and the underlying rough surface that masks its response. We also think that T1's quite high-incidence angle value of 70 deg and its small size in wavelength-scale might be the other cause of relatively smaller backscattered response compared to other TCRs. As for the square-type TCR (T5), it can only be recognized in  $|S_{\text{HH}}|$  with low intensity because of the surrounding grass

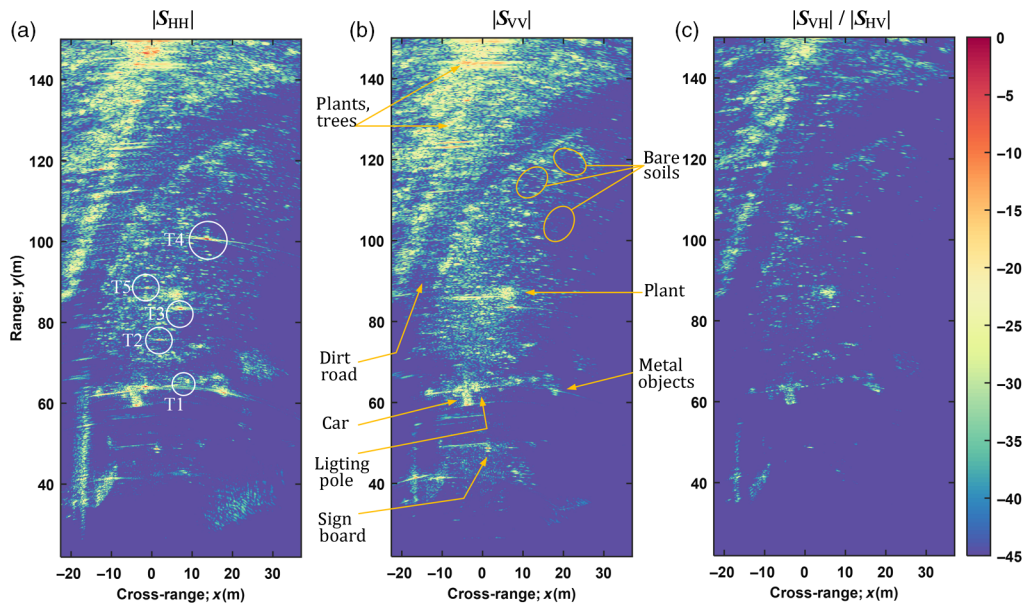


**Fig. 4** Measured (a)  $|S_{HH}|$ , (b)  $|S_{VV}|$ , and (c)  $|S_{VH}|/|S_{HV}|$  images for the test site. The locations of corner reflectors are marked with white circle.

medium. Regarding the cross-polar responses, intensity levels are nonzero owing to the diffraction from the edges of the TCRs but low enough to be indiscernible from the natural environment, as one would expect.

Second, the characteristics of manmade items are examined as follows: these objects are positioned at near ranges around the parking lot, which has a concrete surface bordered by paving stones (see Fig. 3). The surface appears to have very low intensities due to specular reflections. The edge facing to the radar acts like a dihedral corner reflector and thus yields predominantly nondepolarizing (i.e., deterministic) reflection characteristics, as seen from the co-polar images. A certain amount of energy can also be noticed in  $|S_{VH}|$ , which can be attributed to the grasses and plants existing along the edges. The other targets can be distinguished as hot spots in all polarization images; however, they have higher power levels for the  $|S_{HH}|$  case. This situation is more evident especially for the car, lighting pole, and two vertical metal structures as seen in Fig. 4. Depolarizing objects offering relatively high cross-polarized returns are the car and the metal objects that have complex geometries. These observations validate that the radar returns of deterministic complex targets are usually stronger and better visualized for the co-polarization channels.

Finally, the polarimetric backscattering signatures of the natural terrain are investigated. At first glance, the different sections can be distinguished in all cases, though slightly less evident within the  $|S_{VH}|$  image. Among these sections are: the dirt road, dense vegetation on the left side of the road, and slightly vegetated middle field. The dirt road and bare soil regions have almost smooth surfaces when the operation wavelengths are concerned [see Eq. (4)], thereby producing specular reflections that are shown up very small intensities. In contrast, the middle field covered with grass and small plants produces reasonable amount of backscattered energy in the form of quasispecular surface and/or volume scattering components. Accordingly, it has slightly larger intensities. The strongest reflections are emerged from the trees and rather large plants owing to single and multiple scattering mechanisms as expected.

Figure 5(a) shows the  $|S_{HH}|$  image zoomed in the area of reflector targets aimed for the resolution analysis. The range and cross-range cuts as well as the  $-4$  dB contour plot were extracted through the peak of the T2's data as shown in Figs. 5(b)–5(d). The resultant measured  $-4$  dB range and cross-range resolutions were found to be 19 and 58.6 cm, whereas the theoretical values for a center wavelength value of  $\lambda_c = 20$  cm and  $R = 75.5$  m are 10 and 57 cm, respectively.

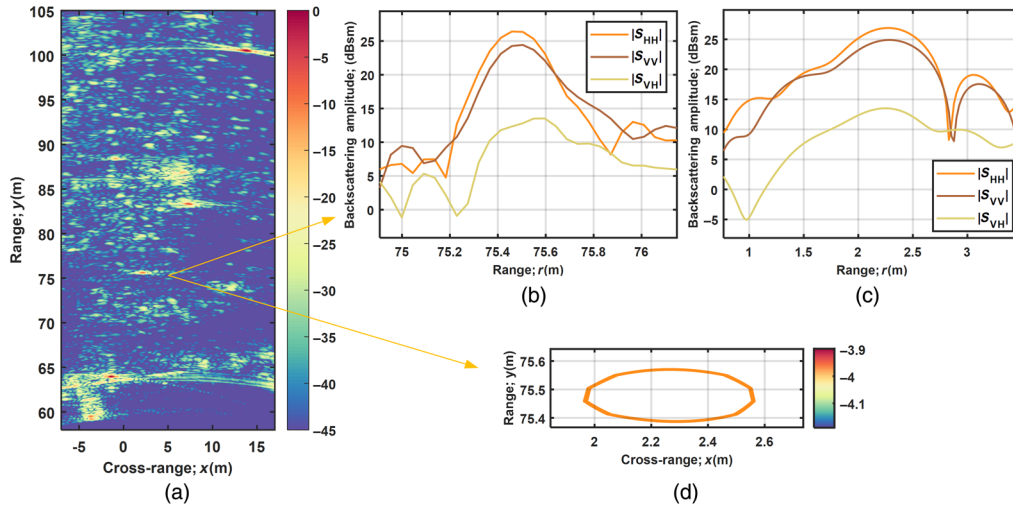


**Fig. 5** Resolution analysis: (a)  $|S_{HH}|$  image zoomed in to TCR targets, (b) range cut, (c) cross-range cut, and (d)  $-4$  dB contour plot, through the peak of T2's image data.

## 4.2 Pauli RGB Image

The Pauli RGB image is obtained by constructing the three element scattering vector  $\vec{k}_{3P}$  defined in Pauli basis as

$$\vec{k}_{3P} = \frac{1}{\sqrt{2}} [S_{HH} + S_{VV}, S_{HH} - S_{VV}, 2S_{VH}]^T, \quad (6)$$

and then assigning blue, red, and green colors to the amplitudes of the first, second, and third components, respectively. Blue ( $|S_{HH} + S_{VV}|$ ) represents isotropic “odd-bounce” scattering such as caused by TCRs or single-bounce scattering from rough surfaces like grassy areas. Red ( $|S_{HH} - S_{VV}|$ ) indicates isotropic “even bounce” scattering such as observed from dihedral corner reflection formed by ground-wall structures. Green ( $2|S_{HV}|$ ) can be interpreted as the volume scattering contribution such as from trees or isotropic even bounce scattering from 45-deg oriented targets.

Figure 6 shows the Pauli RGB image of the investigated scene for the full range and zoomed in the regions of manmade targets. The vegetated areas and complex manmade targets are mostly seen in green tones due to relatively high intensity of the VH channel that is typically associated with volume or multiple scattering. The changes in the intensity of green color are strongly related to the relative contribution of the other, namely odd and even-bounce components. As an example, the top left corner of the image contains relatively dense vegetation of grassy regions and trees, which appear as brighter green due to a combination of odd, even, and volume scattering events. Note that microwaves around L-band are better able to penetrate the trees and interact with their structural components such as leaves, branches, and trunks thereby giving rise to a mixture of such scattering mechanisms. On the other hand, unvegetated areas such as dirt road are shown by dark areas in the image as a result of specular reflection. As can be noticed from the zoomed image, TCRs are shown up as white (i.e., blue + red + green) and magenta (i.e., blue + red) tones indicating a blend of different scattering component returns. This may be due to the interaction of the electromagnetic wave with nonideal ground conditions and also the lack of full-polarimetric calibration. The backscatter from unnatural ground targets (car, metal objects, lighting pole, and signboard) includes all types of scattering as indicated by green, white, yellow, and red colors. Moreover, the paving stones facing to the radar, car's front part, lighting pole, and signboard, all tend to have a high portion of double-bounce scattering because of the dihedral structure formed with the ground-plane. In summary, these observations confirm that Pauli decomposition enables only isotropic scattering (i.e.,  $|S_{HH}| = |S_{VV}|$ ) mechanisms and thus better represents the targets whose orientations exhibit this property.

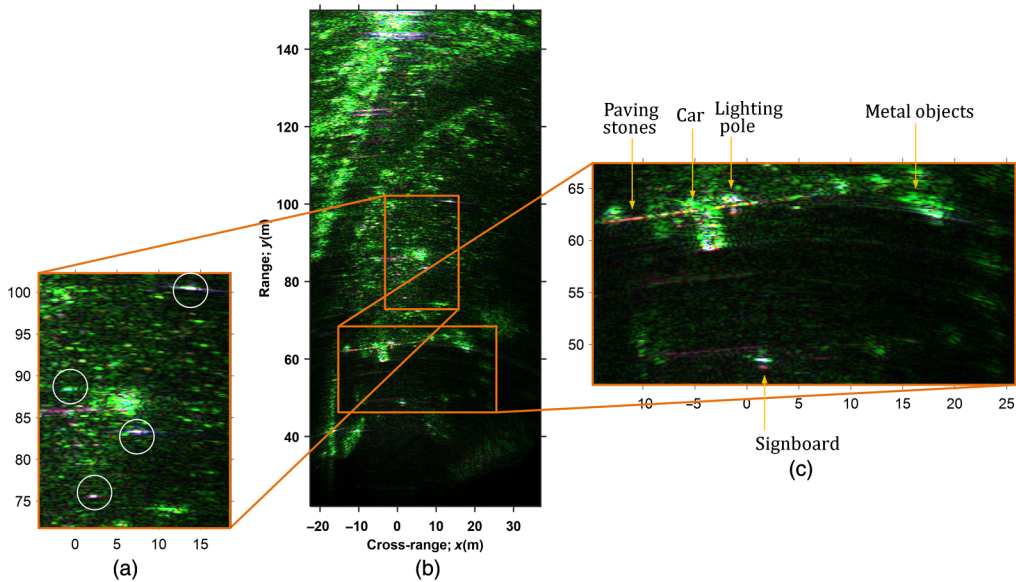


**Fig. 6** (a) Pauli RGB image of the test site for full range, (b) zoomed around reflector targets, and (c) parking lot region (right). The locations of the reflectors are marked with white circle.

### 4.3 Eigenvector/Eigenvalue-Based Decomposition

We have employed the well-known eigenvector and eigenvalue-based decomposition developed by Cloude and Pottier.<sup>55,59</sup> The  $3 \times 3$  polarimetric coherency matrix  $[T_3]$  was formed from the outer product of the Pauli scattering vector  $\vec{k}_{3P}$  and averaged over a  $5 \times 5$  window. The resulting matrix  $\langle [T_3] \rangle$  was expressed in a diagonal form as

$$\langle [T_3] \rangle = [E_3] \begin{bmatrix} \lambda_1 & 0 & 0 \\ 0 & \lambda_2 & 0 \\ 0 & 0 & \lambda_3 \end{bmatrix} [E_3]^{-1}, \quad (7)$$

where  $\langle \dots \rangle$  indicates spatial averaging,  $\lambda_1 \geq \lambda_2 \geq \lambda_3 \geq 0$  are eigenvalues, and  $[E_3] = [\vec{e}_1 \ \vec{e}_2 \ \vec{e}_3]$  is the unitary eigenvector matrix with columns corresponding to the complex eigenvectors  $\vec{e}_1$ ,  $\vec{e}_2$ , and  $\vec{e}_3$ . By performing this decomposition, the  $\langle [T_3] \rangle$  matrix, which is in general of rank 3, can be written as the sum of three independent scattering processes as

$$\langle [T_3] \rangle = \sum_{i=1}^3 \lambda_i \vec{e}_i \cdot \vec{e}_i^+ = [T_a] + [T_b] + [T_c], \quad (8)$$

where the superscript  $+$  indicates the conjugate transpose operation. Each of  $[T_a]$ ,  $[T_b]$ , and  $[T_c]$  matrices is of rank 1, describing a deterministic scattering process. The eigenvalues quantify the power of each contribution, whereas the form of the eigenvectors determines the type of scattering.

Figure 7 shows the total power images of these three scattering mechanisms for the investigated scene. Figure 7(a) shows the first component  $[T_a]$  corresponds to the largest eigenvalue ( $\lambda_1$ ) represents the dominant scattering mechanism occurring. As obvious from this figure, anisotropic surface and other dominant scattering targets are well localized as hot spots in the image. Figures 7(b) and 7(c) show the second component  $[T_b]$  and the third component  $[T_c]$ , respectively. These components represent secondary dihedral and/or multiple scattering contributions, respectively. The images in Figs. 7(b) and 7(c) clearly illustrate that the fields covered with vegetation, trees, and complex manmade targets have significant secondary scattering contributions indicating depolarizing scattering process. On the other hand, for TCRs and targets with simple geometries such as the lighting pole and signboard, the contribution of the second and

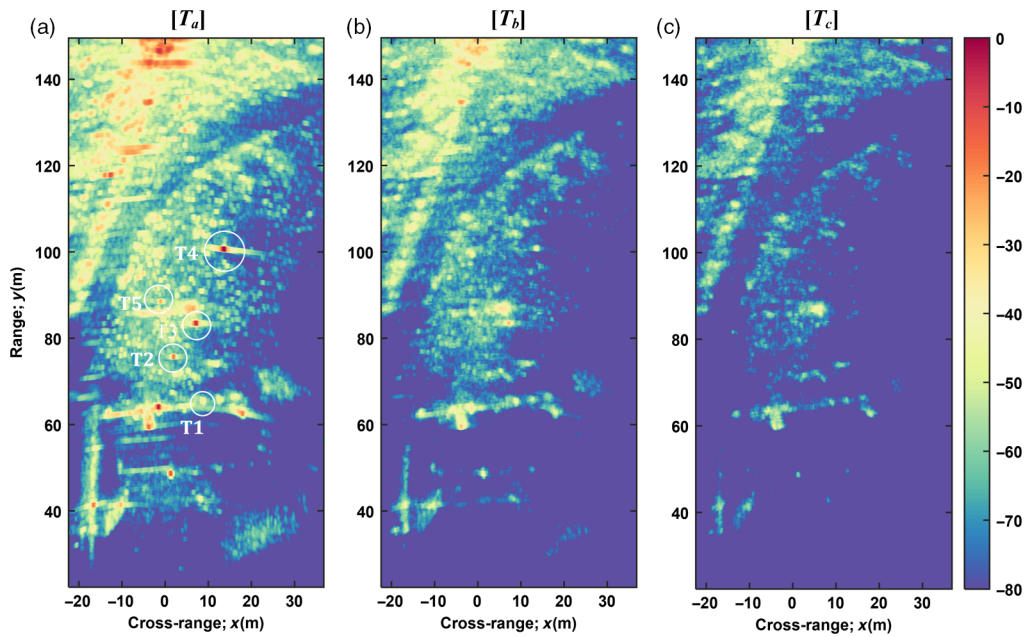


**Fig. 7** Total power images of the three scattering mechanisms obtained by applying the eigen-based decomposition on the L-band data of the test site: (a) the first component ( $T_a$ ), (b) the second component ( $T_b$ ), and (c) the third component ( $T_c$ ).

third components is much lower than the first component implying a dominance of nondepolarizing scattering.

The parameters of the total power TP, polarimetric scattering entropy ( $H$ ), and mean alpha angle ( $\bar{\alpha}$ ) were then extracted and plotted as shown in Fig. 8. The sum of the three eigenvalues gives the total power TP received from the scatterer, which is also known as the span. For natural terrain, higher intensities in TP images may be interpreted as the regions where secondary scatterings occur. This can be verified from Fig. 8(a), which indicates high power values for larger plants and trees due to L-band multiple scattering from a heterogeneous medium. The car and the metal structure are also recognized as strong scatterers because of their high co- and cross-polarized backscatter. For the TCRs, signboard and lighting pole, high co-polarized returns make them clearly noticeable in the power image shown in Fig. 8(a).

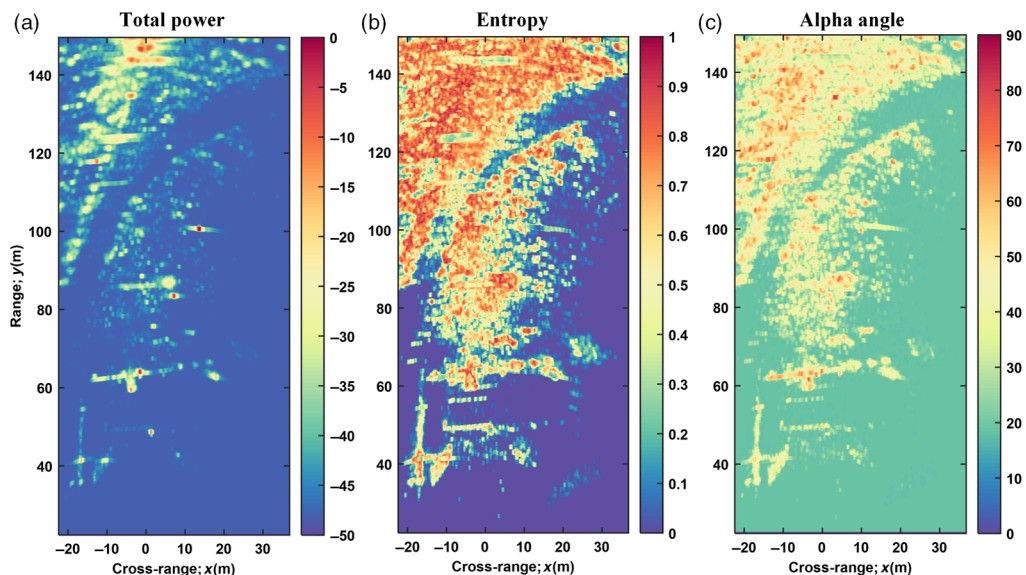


**Fig. 8** (a) Total power, (b) entropy, and (c) alpha angle maps for the test site.

The degree of randomness of scattering is determined by the polarimetric scattering entropy  $H$ , which ranges from 0 to 1 and represents the eigenvalue information in  $\langle [T_3] \rangle$ . An entropy of 0 describes a nondepolarizing scattering, whereas an entropy value of 1 represents a fully depolarizing scattering. From Fig. 8(b), it is clear that entropy rises with increasing vegetative component over the soil, as well as increasing structural complexity of the manmade targets. These media or high  $H$  values are characteristic for the presence of two or more scattering mechanisms.

As mentioned above, the types of the scattering mechanisms represented by  $[T_a]$ ,  $[T_b]$ , and  $[T_c]$  are given by the corresponding eigenvectors. The mean alpha angle is an average representation of this eigenvector information and can be used to identify the underlying average scattering mechanism. It is a continuous parameter ranging from 0 deg to 90 deg; in general,  $0 \text{ deg} \leq \bar{\alpha} \leq 30 \text{ deg}$ ,  $40 \text{ deg} \leq \bar{\alpha} \leq 50 \text{ deg}$ , and  $60 \text{ deg} \leq \bar{\alpha} \leq 90 \text{ deg}$  correspond to surface, dipole, and dihedral scatterings, respectively. Figure 8 shows the variations in  $\bar{\alpha}$  values for the investigated scene with the color scale between (0 deg, 90 deg) shown on the right. The double-bounce returns from the car, paving stones facing to the radar, lighting pole, and relatively large plants and trees exhibit dihedral scattering in red color between 60 deg and 80 deg. The single bounce returns from the metal structure and surfaces with low vegetation cover show the typical dipole scattering characteristics with  $\bar{\alpha}$  around 45 deg. In addition, the dirt road and surfaces of bare or almost bare soil have  $\bar{\alpha}$  values below 30 deg indicating less anisotropic surface scattering. The results indicate that  $\bar{\alpha}$  parameter is especially useful in characterizing scattering mechanisms for manmade structures since it can be used to distinguish different scattering mechanisms of surface, dipole, and dihedral.

#### 4.4 Classification in the $H/\bar{\alpha}$ Space

The entropy ( $H$ ) and mean alpha ( $\bar{\alpha}$ ) values derived from the eigendecomposition of the coherency matrix can be used for classification purposes. An unsupervised  $H/\bar{\alpha}$  classification was performed to further interpret the observed backscatterings. Cloude and Pottier<sup>59</sup> proposed a subdivision of the plane into nine classes (eight usable) for L-band, in order to separate the data into basic scattering mechanisms. We adopted this classification scheme whose scattering classes with their partitioning and descriptions are given in Fig. 9.

As an initial validation, scatter plots showing the distribution of the measured data over the space are examined. Figure 10 shows examples of these plots for a variety of target regions, which are indicated on the  $|S_{HH}|$  image. In Fig. 10(a), the measured  $|S_{HH}|$  image of the test site is provided. The selected manmade targets, namely the TCR, paving stones, and lighting pole, are expected to lie in the classes of low-entropy surface scattering (C8), multiple (even-bounce) scattering (C6), and low-entropy dipole scattering (C7), respectively. These targets are observed to be within the true classes. At L-band, the relatively large-sized plant (see Fig. 3) might be predicted to have medium entropy scattering with the dominant scattering mechanisms being dipole and/or double-bounce. The corresponding plot in Fig. 10 leads to C3 and C4 classification, which is in good agreement with this prediction. Therefore, as is easily seen from Fig. 10(b), the  $H/\bar{\alpha}$  characteristics of the image are highly concentrated in C8 region and some of the characteristics are distributed along C5 region. Based on the descriptions from Fig. 9, the C8

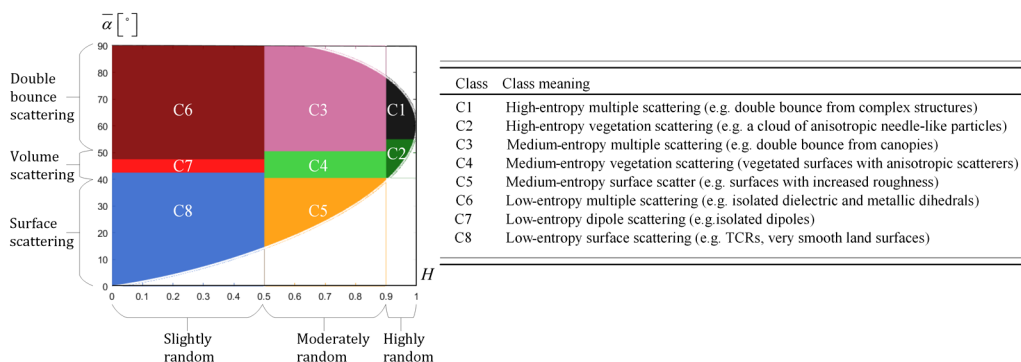
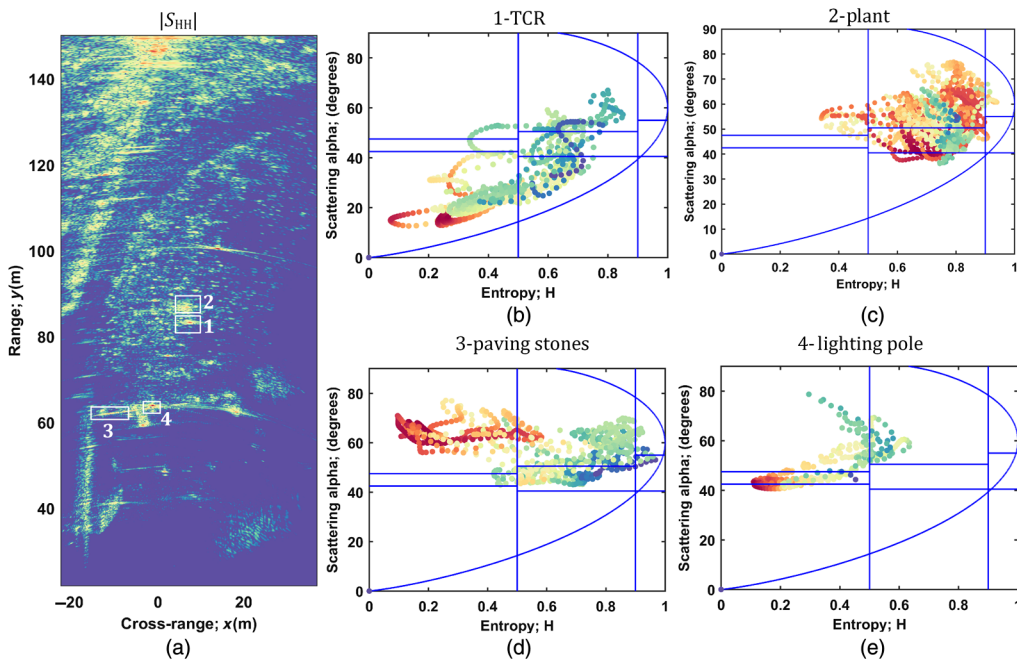


Fig. 9 The  $H/\bar{\alpha}$  plane with classes (C1)–(C8) and their partitioning and descriptions.<sup>59</sup>



**Fig. 10** Scatter plots showing the distribution of values in the  $H/\bar{\alpha}$  classification space. The selected target regions are indicated on the  $|S_{HH}|$  image with white rectangles and numbers: (a) measured  $|S_{HH}|$  image of the test site, (b) TCR, (c) plant, (d) paving stones, and (e) lighting pole.

provides low-entropy surface scattering such as TCRs that is in parallel with the  $H/\bar{\alpha}$  result we got. During the experiment, the TCR was put on a rough grassy surface (C5), which is why we see some energy distributions in the  $H/\bar{\alpha}$  image of Fig. 10(b). The selected region that contains a plant (a small tree) in Fig. 10(a) has produced an  $H/\bar{\alpha}$  image of Fig. 10(c) that is highly concentrated in C4. This result is also well-matched with the descriptions in Fig. 9, in which C4 usually represents vegetated surfaces with anisotropic scatterers. The region #3 that contained some paving stones constituted an  $H/\bar{\alpha}$  image of Fig. 10(d) mainly focused within C6 region. C6 in  $H/\bar{\alpha}$  plane generally contains double-bounce mechanisms. As for the paving stones, this result is expected since they form a kind of dihedrals for the look angle of our radar. For the last test region that contained the lighting pole, corresponding  $H/\bar{\alpha}$  image is plotted in Fig. 10(e), where most of the energy is framed within C7 region. Since the lighting pole behaves like a dipole, it is naturally expected to see its  $H/\bar{\alpha}$  image in C7 based on the descriptions in Fig. 9. Overall, this analysis clearly demonstrates us that  $H/\bar{\alpha}$  plane can be used to extract different features of the scene with high fidelity and accuracy.

The  $H/\bar{\alpha}$  classification result for the whole image is shown in Fig. 11 (see also Fig. 9 for the color of each class). Some pixels belonging to the trees, plants, and bushes are classified as C3, medium entropy multiple (double) bounce scattering, which is more pronounced for areas of relatively dense vegetation. This is consistent with expectation since L-band waves can sufficiently penetrate the canopy, producing double-bounce mechanisms associated with trunk-ground interactions. As the scale of the vegetation cover decreases (i.e., grassy fields), the contribution of double-bounce signatures reduces and these areas appear to have dipole or surface scattering characteristics with the corresponding classification results of C4 and C5, respectively. Moreover, the smooth sections of the dirt road, bare soil regions, as well as TCR targets are correctly classified as C8, although they are masked with background blue color.

As for the manmade targets, the car is recognized to have each type of medium entropy classes of C3, C4, and C5. This can be attributed to its anisotropic structure that gives rise to high polarimetric randomness when radar is not facing to the dominant scattering directions. The car body is packed of localized anisotropic scattering centers with correlated orientations, which can generate moderate  $H$  values. This also reflects the inability of  $H/\bar{\alpha}$  classification to distinguish between anisotropic and isotropic targets that have the same scattering properties.

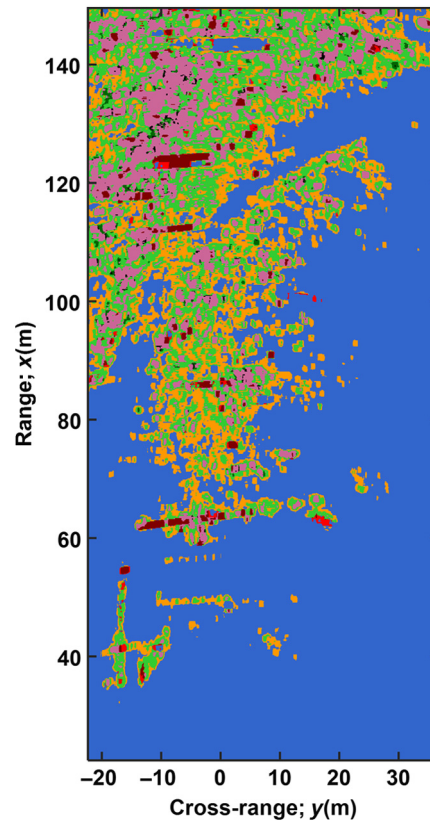


Fig. 11  $H/\bar{\alpha}$  classification result.

In addition, the front part of the car and paving stones have azimuthal alignments that generate dominant double-bounce scattering, and thus both are classified into low-entropy C6 class. Finally, the lightning pole and metal structures, which both have predominant dipole scattering, are correctly classified as C7.

## 5 Conclusion

An experimental assessment of polarimetric L-band backscattering was made through the GB-SAR data of a test site consisting of a typical vegetated terrain and various manmade targets based on two main polarization interpretation schemes, namely amplitude-based interpretation and target decomposition-based interpretation. By applying the suggested polarimetric characterization methodology, the polarimetric L-band GB-SAR image signatures were characterized via examination of intensity images in terms of the backscattering mechanisms and their dependency on frequency, polarization, and look angle, the Pauli RGB image, some polarimetric parameters derived from the eigendecomposition of the coherency matrix and distribution of values in the  $H/\bar{\alpha}$  plane and  $H/\bar{\alpha}$  classification results.

Interpretation of the amplitude data demonstrated that co-polarized and cross-polarized SAR images of the scene constitute a basis analysis for the polarimetric investigation of the targets and their scattering feature characteristics. On the other hand, the combined usage of the Pauli decomposition, the eigenvalue/eigenvector decomposition, and the  $H/\bar{\alpha}$  classification together with the variation in the relevant polarimetric parameters can provide a methodological analysis for the identification and classification of scattering mechanisms. In Fig. 6, for instance, the Pauli decomposition image of the terrain can especially distinguish between isotropic odd-bounce and even-bounce scattering contributions. The TCRs and dihedrals are good examples for the targets that support these scattering characteristics.

A more detailed interpretation of the data has been given using the eigenvalue/eigenvector decomposition of the coherency matrix. The total power images of the single components of the eigen-based decomposition can easily reveal the scattering contributions from the first and

secondary (depolarizing) scattering mechanisms. A good example for this analysis is presented in Fig. 7 where scattering features from TCRs, dihedrals, and regions with vegetation and trees can be successfully distinguished due to the differences in their entropy values. Other polarization interpretation schemes based on this decomposition that we have utilized are entropy ( $H$ )-based and mean-alpha ( $\bar{\alpha}$ ) based interpretations. In Fig. 10, we have demonstrated that  $H/\bar{\alpha}$  space can be used as the basis to characterize the scattering types from various targets either natural or manmade. While the value of  $H$  is controlling the randomness of the scattering, that of  $\bar{\alpha}$  provides the types of scattering. Therefore, the conducted analyses of the  $H/\bar{\alpha}$  image of the scene provided very good predictions on the scattering features of the objects in terms of the type and the feature.

The  $H/\bar{\alpha}$  classification image given in Fig. 11 provided useful information as confirmed by the correct classification of both natural and artificial targets. The artificial targets such as the lighting pole, complex metallic objects, paving stones, and others were seen to be classified in the predicted scattering zones. The car was observed to occupy multiple zones of medium entropy, indicating different kinds of scattering mechanisms, owing to its complex structure. As for the natural media, medium entropy scatterings were mostly observed together with varying scattering mechanisms that depends on the density, size, and structure of the vegetation. In general, the obtained results confirm the underlying scattering mechanisms and also the validity of the  $H/\bar{\alpha}$  classification for this high-resolution image data. Despite this, the comparison of the results for trees and the car target revealed that the  $H/\bar{\alpha}$  classification scheme is unable to distinguish between isotropic and anisotropic targets, which have similar polarimetric scattering properties.

## Acknowledgments

This work was supported in part by Mersin University Scientific Research Unit under Grant No. 2017-1-TP3-2129.

## References

1. A. Moreira et al., "A tutorial on synthetic aperture radar," *IEEE Geosci. Remote Sens. Mag.* **1**(1), 6–43 (2013).
2. K. Ouchi, "Recent trend and advance of synthetic aperture radar with selected topics," *Remote Sens.* **5**(2), 716–807 (2013).
3. R. Zoughi, L. K. Wu, and R. K. Moore, "Identification of major backscattering sources in trees and shrubs at 10 GHz," *Remote Sens. Environ.* **19**(3), 269–290 (1986).
4. K. V. Chet, C. B. Kuan, and C. H. Teik, "Development of a ground-based radar for scattering measurements," *IEEE Antennas Propag. Mag.* **45**(2), 36–42 (2003).
5. C. Albinet et al., "TropiSCAT: a ground based polarimetric scatterometer experiment in tropical forests," *IEEE J. Sel. Top. Appl. Earth Obs. Remote Sens.* **5**(3), 1060–1066 (2012).
6. Y. Inoue et al., "Season-long daily measurements of multifrequency (Ka, Ku, X, C, and L) and full-polarization backscatter signatures over paddy rice field and their relationship with biological variables," *Remote Sens. Environ.* **81**(2–3), 194–204 (2012).
7. L. He et al., "Polarimetric analysis of radar backscatter from ground-based scatterometers and wheat biomass monitoring with advanced synthetic aperture radar images," *J. Appl. Remote Sens.* **10**(2), 026008 (2016).
8. B.-L. Cho et al., "Automobile-based SAR/InSAR system for ground experiments," *IEEE Geosci. Remote Sens. Lett.* **3**(3), 401–405 (2006).
9. J. T. Gonzalez-Partida et al., "Ground SAR system with tunable distance limits and low sampling rate," in *IET Int. Conf. Radar Syst.*, Edinburgh, pp. 1–5 (2007).
10. J.-T. Gonzalez-Partida et al., "SAR system for UAV operation with motion error compensation beyond the resolution cell," *Sensors* **8**(5), 3384–3405 (2008).
11. C. H. Jung, J.-H. Song, and H.-C. Lee, "Experimental X-band automotive SAR system for land observation application," in *Seventh Int. Conf. Adv. Satell. and Space Commun.*, Barcelona, Spain, pp. 90–93 (2015).

12. M. Pieraccini, G. Luzi, and C. Atzeni, "Ground-based interferometric SAR for terrain elevation mapping," *Electron. Lett.* **36**(16), 1416–1417 (2000).
13. M. Pieraccini, G. Luzi, and C. Atzeni, "Terrain mapping by ground-based interferometric radar," *IEEE Trans. Geosci. Remote Sens.* **39**(10), 2176–2181 (2001).
14. G. Nico et al., "Ground-based SAR interferometry for terrain mapping: theory and sensitivity analysis," *IEEE Trans. Geosci. Remote Sens.* **42**(6), 1344–1350 (2004).
15. G. Nico et al., "Generation of digital terrain models with a ground-based SAR system," *IEEE Trans. Geosci. Remote Sens.* **43**(1), 45–49 (2005).
16. D. Leva et al., "Temporal analysis of a landslide by means of a ground-based SAR interferometer," *IEEE Trans. Geosci. Remote Sens.* **41**(4), 745–752 (2003).
17. D. Tarchi et al., "Monitoring landslide displacements by using ground-based synthetic aperture radar interferometry: application to the Ruinon landslide in the Italian Alps," *J. Geophys. Res.* **108**(B8), 1–14 (2003).
18. A. Aguasca et al., "A solid state L to X-band flexible ground-based SAR system for continuous monitoring applications," in *IEEE Int. Geosci. and Remote Sens. Symp.*, Anchorage, Alaska, pp. 757–760 (2004).
19. G. Luzi et al., "Ground-based radar interferometry for landslides monitoring: atmospheric and instrumental decorrelation sources on experimental data," *IEEE Trans. Geosci. Remote Sens.* **42**(11), 2454–2466 (2004).
20. G. Bernardini, P. Ricci, and F. Coppi, "A ground based microwave interferometer with imaging capabilities for remote measurements of displacements," in *Proc. 7th Geomatic Week*, Barcelona, Spain (2007).
21. D. Tarchi et al., "SAR imaging with noise radar," *IEEE Trans. Aerosp. Electron. Syst.* **46**(3), 1214–1225 (2010).
22. S. Rödelsperger, "Real-time processing of ground based synthetic aperture radar (GB-SAR) measurements," PhD Dissertation, Technische Universität Darmstadt, Darmstadt, Germany (2011).
23. O. Monserrat, "Deformation measurement and monitoring with ground-based SAR," PhD Dissertation, Institute of Geomatics, Barcelona, Spain (2012).
24. O. Monserrat, M. Crosetto, and G. Luzi, "A review of ground-based SAR interferometry for deformation measurement," *ISPRS J. Photogramm. Remote Sens.* **93**, 40–48 (2014).
25. M. Crosetto et al., "Discontinuous GBSAR deformation monitoring," *ISPRS J. Photogramm. Remote Sens.* **93**, 136–141 (2014).
26. L. Pipia, "Polarimetric differential SAR interferometry with ground-based sensors," PhD Dissertation, Universitat Politècnica de Catalunya, Barcelona, Spain (2009).
27. L. Pipia et al., "Polarimetric differential SAR interferometry: first results with ground-based measurements," *IEEE Geosci. Remote Sens. Lett.* **6**(1), 167–171 (2009).
28. L. Pipia et al., "Polarimetric temporal analysis of urban environments with a ground-based SAR," *IEEE Trans. Geosci. Remote Sens.* **51**(4), 2343–2360 (2013).
29. R. Iglesias et al., "Ground-based polarimetric SAR interferometry for the monitoring of terrain displacement phenomena—Part I: theoretical description," *IEEE J. Sel. Top. Appl. Earth Obs. Remote Sens.* **8**(3), 980–993 (2015).
30. R. Iglesias et al., "Ground-based polarimetric SAR interferometry for the monitoring of terrain displacement phenomena—Part II: applications," *IEEE J. Sel. Top. Appl. Earth Obs. Remote Sens.* **8**(3), 994–1007 (2015).
31. M. L. Cuenca, "Contribution to ground-based and UAV SAR systems for Earth observation," PhD Dissertation, Universitat Politècnica de Catalunya, Barcelona, Spain (2017).
32. S. Baffelli et al., "Polarimetric calibration of the Ku Band advanced polarimetric radar interferometer (KAPRI)," *IEEE Trans. Geosci. Remote Sens.* **56**(4), 2295–2311 (2018).
33. T. G. Yitayew, L. Ferro-Famil, and T. Eltoft, "High resolution three-dimensional imaging of sea ice using ground-based tomographic SAR data," in *Proc. Eur. Conf. Synth. Aperture Radar*, Berlin, Germany, pp. 1–4 (2014).
34. L. Ferro-Famil et al., "3-D SAR imaging of the snowpack at X- and Ku-band: results from the AlpSAR campaign," in *Proc. Eur. Conf. Synth. Aperture Radar*, Berlin, Germany, pp. 1–4 (2014).

35. O. Frey, C. L. Werner, and A. Wiesmann, "Tomographic profiling of the structure of a snow pack at X-/Ku-band using SnowScat in SAR mode," in *Eur. Radar Conf.*, Paris, France, pp. 21–24 (2015).
36. H. Wang et al., "Monitoring bare agricultural soil: comparison between ground based SAR PoSAR system measurements and multi-angular RADARSAT-2 datasets," in *10th Eur. Conf. Synth. Aperture Radar*, Berlin, Germany, pp. 1–4 (2014).
37. H. Wang et al., "Multi-angular ground-based SAR system for soil surface roughness characterization," *Electron. Lett.* **51**(15), 1197–1199 (2015).
38. S. C. M. Brown et al., "High-resolution measurements of scattering in wheat canopies—implications for crop parameter retrieval," *IEEE Trans. Geosci. Remote Sens.* **41**(7), 1602–1610 (2003).
39. K.-S. Lim and V.-C. Koo, "Design and construction of wideband VNA ground-based radar system with real and synthetic aperture measurement capabilities," *Prog. Electromagn. Res.* **86**, 259–275 (2008).
40. K. Morrison and M. L. Williams, "High resolution PolInSAR with the ground-based SAR (GB-SAR) system: measurement and modelling," in *Proc. IEEE Int. Geosci. and Remote Sens. Symp.*, Seoul, South Korea, pp. 1105–1108 (2005).
41. J. F. Penner and D. G. Long, "Ground-based 3-D radar imaging of trees using a 2-D synthetic aperture," *Electronics* **6**, 11 (2017).
42. Z. S. Zhou, "Application of a ground-based polarimetric SAR system for environmental study," PhD Dissertation, The Graduate School of Engineering, Tohoku University, Sendai, Japan (2003).
43. Z. S. Zhou, "Development of a ground-based polarimetric broadband SAR system for non-invasive ground-truth validation in vegetation monitoring," *IEEE Trans. Geosci. Remote Sens.* **42**(9), 1803–1810 (2004).
44. D. H. T. Minh et al., "Vertical structure of P-band temporal decorrelation at the Paracou forest: results from TropiScat," *IEEE Geosci. Remote Sens. Lett.* **11**(8), 1438–1442 (2014).
45. H. Lee et al., "Development of a GB-SAR (II): focusing algorithms," *Korean J. Remote Sens.* **23**(4), 247–256 (2007).
46. H. Lee et al., "Development of a truck-mounted arc-scanning synthetic aperture radar," *IEEE Trans. Geosci. Remote Sens.* **52**(5), 2773–2779 (2014).
47. H. Lee et al., "Development a GB-SAR (I): system configuration and interferometry," *Korean J. Remote Sens.* **23**(4), 237–245 (2007).
48. M.-K. Kang et al., "Preliminary results of polarimetric characteristics for C-band quad-polarization GB-SAR images using H/A/ $\alpha$  polarimetric decomposition theorem," *Korean J. Remote Sens.* **25**(6), 531–546 (2009).
49. H. Lee, Y. Ji, and H. Han, "Experiments on a ground-based tomographic synthetic aperture radar," *Remote Sens.* **8**(8), 667 (2016).
50. Y. Ji, H. Han, and H. Lee, "Construction and application of tomographic SAR system based on GB-SAR system," in *IEEE Int. Geosci. and Remote Sens. Symp.*, Quebec, QC, Canada, pp. 1891–1894 (2014).
51. S. Xing et al., "Three-dimensional reconstruction of man-made objects using polarimetric tomographic SAR," *IEEE Trans. Geosci. Remote Sens.* **51**(6), 3694–3705 (2013).
52. P. J. Ferrer et al., "Transpolarising trihedral corner reflector characterisation using a GB-SAR system," *IEEE Geosci. Remote Sens. Lett.* **8**(4), 774–778 (2011).
53. J. Lee and E. Pottier, *Polarimetric Radar Imaging: From Basics to Applications*, CRC Press, Boca Raton, Florida (2009).
54. S. R. Cloude, *Polarisation Application in Remote Sensing*, Oxford University Press, New York (2010).
55. S. Cloude and E. Pottier, "A review of target decomposition theorems in radar polarimetry," *IEEE Trans. Geosci. Remote Sens.* **34**(2), 498–518 (1996).
56. S. W. Chen et al., "Advanced polarimetric target decomposition," in *Target Scattering Mechanism in Polarimetric Synthetic Aperture Radar*, S. W. Chen et al., Eds., pp. 43–106, Springer, Singapore (2018).
57. V. Alberga et al., "Potential of coherent decompositions in SAR polarimetry and interferometry," in *IEEE Int. Geosci. and Remote Sens. Symp.*, Anchorage, Alaska (2004).

58. S. W. Chen et al., "Modeling and interpretation of scattering mechanisms in polarimetric synthetic aperture radar: advances and perspectives," *IEEE Signal Process. Mag.* **31**, 79–89 (2014).
59. S. R. Cloude and E. Pottier, "An entropy based classification scheme for land applications of polarimetric SAR," *IEEE Trans. Geosci. Remote Sens.* **35**(1), 68–78 (1997).
60. MATLAB, Release 2018a, The MathWorks, Inc., Natick, Massachusetts, <http://www.mathworks.com/products/matlab/>, accessed (2019).
61. C. Ozdemir et al., "A review on migration methods in B-scan ground penetrating radar imaging," *Math. Probl. Eng.* **2014**, 1–16 (2014).
62. S. Demirci et al., "A study on millimeter-wave imaging of concealed objects: application using back-projection algorithm," *Prog. Electromagnet. Res.* **128**, 457–477 (2012).

**Sevket Demirci** received his BS degree from Cukurova University, Adana, Turkey, and his MS and PhD degrees from Mersin University, Mersin, Turkey, in 1998, 2005, and 2013, respectively, all in electrical and electronics engineering. Currently, he is an assistant professor in the Department of Electrical and Electronics Engineering at Mersin University. His current research interests include radar engineering, synthetic aperture radar (SAR), ground penetrating radar (GPR), polarimetric SAR, target detection techniques, and compressive sensing.

**Betul Yilmaz** received her BS degree in 2005 from Erciyes University, Kayseri, Turkey, and her MSE and PhD degrees in electrical and electronics engineering from Mersin University in 2008 and 2017, respectively. She is an assistant professor in the Department of Electrical and Electronics Engineering at Mersin University. Her current research interests include radar imaging, through-wall radar, inverse synthetic aperture radar (ISAR), SAR, GPR, and antenna design. She is a recipient of a JARS best paper award for photo-optical instrumentation and design for her paper "Design and prototype of radar sensor with Vivaldi linear array for through-wall radar imaging: an experimental study," which was published in *Journal of Applied Remote Sensing*, Vol. 10(4), 046012 (November 18, 2016).

**Hakan Isiker** received his BS degree from Nigde University, Nigde, Turkey, and his MS degree from Mersin University, Mersin, Turkey, in 2002 and 2007, respectively, both in electrical-electronics engineering. Currently, he is an instructor in the Department of Electronics and Automation at Vocational School of Technical Sciences of Mersin University. His current research interests are passive radar imaging systems, SAR focusing algorithms, image processing, and target detecting techniques.

**Serhat Gökkan** received his BS and MS degrees from Hacettepe University, Ankara, Turkey, in 1999 and 2002, respectively, both in electrical and electronics engineering. Currently, he is a PhD student in the Department of Electrical-Electronics Engineering at Mersin University. His research interests are radar engineering and obstacle penetrating radar.

**Caner Ozdemir** received his BSEE degree in 1992 from Middle East Technical University, Ankara, Turkey, and his MSE and PhD degrees in electrical and computer engineering from the University of Texas at Austin in 1995 and 1998, respectively. From 1992 to 1993, he worked as a project engineer at the Electronic Warfare Programs Directorate of ASELSAN Electronic Industries Inc., Ankara, Turkey. From 1998 to 2000, he worked as a research scientist at Electronic and Avionics Systems Group, AlliedSignal Inc., Columbia, Maryland, USA. He joined the faculty of Mersin University in 2000 and is currently a professor in the Department of Electrical-Electronics Engineering, Mersin, Turkey. He has been serving as a consultant to the Marmara Research Center of the Scientific and Research Council of Turkey and many defense industry firms. His research interests are radar image/signal processing, ISAR, radar cross section, ground penetrating radar, through-the-wall imaging radar, and antenna design. He has published more than 140 journal articles and conference/symposium papers on these subjects. He is a recipient of URSI EMT-S Young Scientist Award in the 2004 International Symposium on Electromagnetic Theory in Pisa, Italy, and also recipient of a JARS best paper award for photo-optical instrumentation published in the *Journal of Applied Remote Sensing* in 2016. He is the author of the book titled *Inverse Synthetic Aperture Radar Imaging with Matlab Algorithms*.